The biorthogonal decomposition as a tool for investigating fluctuations in plasmas

Thierry Dudok de Wit, A.-l. Pecquet, J.-c. Vallet, R. Lima, A.-L Pecquet, J.-C Valet

The biorthogonal decomposition as a tool for investigating fluctuations in plasmas

T. Dudok de Wit,[a] A.-L. Pecquet, and J.-C. Vallet
Département de Recherches sur la Fusion Contrôlée, Association EURATOM–CEA, Centre d'Etudes Nucléaires de Cadarache, F-13108 Saint-Paul-lez-Durance, France

R. Lima
Centre de Physique Théorique, C.N.R.S. Luminy, Case 907, Unité propre de recherche 7061, F-13288 Marseille cedex 9, France

(Received 1 October 1993; accepted 21 June 1994)

The investigation of fluctuation phenomena in plasmas often necessitates the analysis of spatiotemporal signals. It is shown how such signals can be analyzed using the biorthogonal decomposition, which splits them into orthogonal spatial and temporal modes. The method, also referred to as the singular value decomposition, allows complex spatiotemporal patterns to be decomposed into a few coherent modes that are often easier to interpret. This is illustrated with two applications to fluctuating soft x-ray and magnetic signals, as measured in a tokamak. Emphasis is given to the physical interpretation of the biorthogonal components and their link with known physical models is discussed. It is shown how new insight can be gained in the interpretation of spatiotemporal plasma dynamics.

I. INTRODUCTION

The progress toward a better understanding on fluctuations in plasmas is closely linked to the development of adequate signal processing tools.[1] Spectral-based techniques have so far proven to be indispensable to access signal features that are otherwise not readily observable.[2] Although these techniques can be extremely powerful, they do not always readily apply to spatially extended systems because they are monovariate, i.e., they handle only one variable at a time while freezing the others. The consequence is a deliberate loss of information which may impede a better understanding of the spatiotemporal plasma dynamics. A true description of spatiotemporal signals therefore requires a multivariate analysis.

Most multivariate signal processing techniques have been pioneered by research in the field of fluid dynamics[3–6] where they play an crucial role; some techniques have also originated in other fields such as particle physics.[7] We shall consider here one particular technique called the biorthogonal decomposition (BD) which is essentially an expansion into deterministic functions in time and in space. An early formulation is attributed to Lumley,[3] although several closely related techniques have emerged in other domains. Some of them are the Karhunen–Loève expansion[8] in statistical physics, the proper orthogonal decomposition[9] in probability theory, the principal component analysis[10] in multivariate analysis, and the singular value decomposition (SVD)[11] in numerical linear algebra. The BD[12,13] has originated in the context of nonlinear dynamics, where it has been used to study wave propagations[14] and bifurcations in chaotic systems.[15] The method is formally identical to the SVD but we will keep its terminology, which is more appropriate for our purposes.

Several techniques related to the BD have already been applied in plasma physics, but they were generally used as data reduction tools and not with the aim to examine the spatiotemporal behavior of the plasma. The principal component analysis was used on the Axisymmetric Divertor Experiment (ASDEX)[16,17] and the Rijnhuizen Tokamak Project (RTP)[16,18] tokamaks to reconstruct plasma equilibria and extract plasma parameters. A method related to the principal component analysis was applied to magnetic signals in the High Beta Toroidal Experiment (HBTX1A) reversed-field pinch.[16,19] In a context more in line with our purpose, the SVD was recently used with soft x-ray and magnetic field fluctuations in the Joint European Torus (JET).[16,20] The latter experiment is as far as we know the first to present a space–time analysis of plasma signals.

The purpose of this paper is to use the BD as a heuristic tool to characterize spatiotemporal fluctuations as they are measured in plasmas. A special emphasis will be given to the physical interpretation of the biorthogonal components, which has up to now received little attention. It will be shown how the method can provide new insight into the dynamical behavior of the plasma and furthermore allow some effects to be interpreted in the context of known physical models. To this end, we will consider two applications to signals that have been measured on the Tore Supra[16] tokamak. The outline of this paper is as follows: in Sec. II the method is presented and its differences with respect to other approaches are examined. Some properties of the biorthogonal components are discussed in Sec. III. A first application to magnetohydrodynamic (MHD) fluctuations as observed in the soft x-ray emission is presented in Sec. IV. A second application to the analysis of magnetic field fluctuations follows in Sec. V. The results are discussed in Sec. VI, which also presents some outlooks.

[a]Present address: Laboratoire de Physique et Chimie de Environnement, C.N.R.S., 3A Av. de la Recherche Scientifique, F-45071 Orléans Cedex 2, France.

 1070-664X/94/1(10)/3288/13/$6.00

II. THE BIORTHOGONAL DECOMPOSITION

A detailed analysis of the biorthogonal decomposition and its mathematical properties can be found in Ref. 12. A brief introduction is given here with an emphasis on sampled signals.

We consider a scalar quantity $y(x,t)$ (e.g., electron temperature, electric potential, or magnetic field component) whose time evolution is measured simultaneously at M different spatial locations. The signal is subsequently sampled and the data are assembled into an $N\times M$ matrix Y, in which the columns are time series

$$(\mathsf{Y})_{ij}=y(x_j,t_i) \quad \text{with} \quad i=1,\ldots,N, \quad j=1,\ldots,M. \tag{1}$$

This simple configuration can be generalized to vectorial quantities, to complex signals or to measurements in other (e.g., Fourier) spaces. The biorthogonal expansion consists in expanding the discrete signal $y(x_j,t_i)$ into a set of modes that are orthogonal in time and in space

$$(\mathsf{Y})_{ij}=\sum_{k=1}^{K} A_k\varphi_k(x_j)\psi_k(t_i), \tag{2}$$

with

$$\sum_{i=1}^{N}\psi_k(t_i)\psi_l(t_i)=\sum_{j=1}^{M}\varphi_k(x_j)\varphi_l(x_j)=\delta_{kl}. \tag{3}$$

The finite number of modes $K=\min(N,M)$ determines the global dimension of the data set. Following the nomenclature introduced in Ref. 12, the spatial eigenmodes $\varphi_k(x_j)$ will thereafter be called topos and the temporal eigenmodes $\psi_k(t_i)$ chronos. The weights A_k are either positive or equal to zero and it is conventional to sort the series (2) in decreasing weight order. The BD is unique except when some of the weights are equal; this will be discussed below.

The topos and the chronos are not predefined base functions, in contrast to a Fourier series expansion, but are calculated directly from the data. They satisfy the eigenequations of the two point spatial and temporal scatter matrices of Y

$$\mathsf{S}_x\varphi_k=A_k^2\varphi_k, \quad \text{with} \quad \mathsf{S}_x=\mathsf{Y}^T\mathsf{Y}, \tag{4}$$

$$\mathsf{S}_t\psi_k=A_k^2\psi_k, \quad \text{with} \quad \mathsf{S}_t=\mathsf{Y}\mathsf{Y}^T, \tag{5}$$

where the superscript T denotes transposition. The scatter matrices S_x and S_t do not necessarily have the same size, unless $N=M$. However, they have the same rank and their K largest eigenvalues are identical, the subsequent ones being equal to zero. The positive semidefiniteness of these matrices explains why the weights are also positive or equal to zero. From these eigenequations a physical interpretation of the BD can be given, namely that it projects the data on an orthonormal basis which decorrelates both the time and the space series. Coherent structures such as traveling waves or macroscopic perturbations are significantly correlated in time and in space and should therefore appear more evidently in this new basis.

The BD is in many aspects similar to techniques such as the principal component analysis, which are also based on a decomposition in eigensolutions of Eqs. (4) and (5). The main difference resides in the way the presence of degeneracies in the spectra of the cross-correlation matrices is treated. Degeneracies occur whenever the signal has spatiotemporal symmetries such as traveling waves[21] and thus represent an important feature. Their presence implies the existence of a subset of eigenfunctions which can be arbitrarily chosen, so that the one-to-one correspondence between the spatial and temporal components is lost. In this case, the signal cannot be fully reconstructed from its components. It is well known that signals which have identical scatter matrices are not necessarily identical; this indicates that some information about their space–time behavior is lost in calculating the scatter matrices. The missing information is recovered in the BD by using the isomorphism between the topos and the chronos as an additional constraint to Eqs. (4) and (5):

$$\mathsf{Y}\varphi_k=A_k\psi_k. \tag{6}$$

This one-to-one correspondence, which is in fact a dispersion relation, is an essential feature of the BD, making of it a deterministic tool which treats both space and time dependences simultaneously. Each topo will always correspond to a unique chrono, even when some of the weights are identical. Techniques such as the principal component analysis fail to keep this unique correspondence because they formally treat the spatial and temporal behavior separately.

An important property of the BD and its related techniques is their ability to concentrate most the signal features into a limited set of components only. For any $L\leqslant K$, the truncated expansion

$$(\hat{\mathsf{Y}}_L)_{ij}=\sum_{k=1}^{L} A_k\varphi_k(x_j)\psi_k(t_i) \tag{7}$$

is the best approximation in a least-squares sense of the data matrix Y among all possible sums of L components. In most cases, the weights are strongly ordered and the largest ones exceed the smallest ones by at least an order of magnitude. The components that are associated with large weights represent highly correlated structures and reflect dominant features of the signal. They will be called significant components as opposed to those associated with small weights. The number of significant components has been suggested as a measure of space–time complexity for chaotic systems.[22]

The BD appears here as an efficient data reduction technique which reduces the number of degrees of freedom of the configuration space in which the signal evolves. Its ability to concentrate dominant features into a few spatial and temporal modes makes it well suited for the analysis of spatially extended systems. Before presenting some applications, we proceed by discussing some of the physical inferences that can be made from the biorthogonal components.

III. PROPERTIES OF THE BIORTHOGONAL COMPONENTS

The key to the interpretation of a biorthogonal decomposition is an examination of its weight distribution. This allows one to assess the degree of compressibility of the data

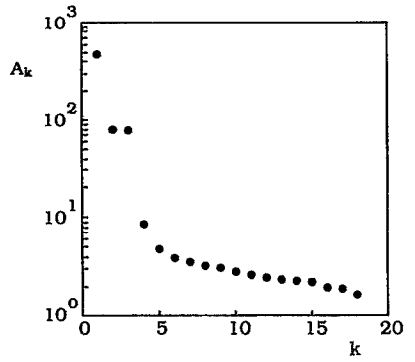

FIG. 1. Simulated weight distribution showing $K=18$ components and three dominant weights.

but also provides valuable information on properties such as spatiotemporal symmetries, linear combinations between signals, etc.

Several parameters allow one to quantify the weight distribution. We first define the global signal energy

$$E=\sum_{i=1}^{N}\sum_{j=1}^{M}(\Upsilon)_{ij}^2, \tag{8}$$

which is equal to the sum of the squared weights

$$E=\sum_{k=1}^{K}A_k^2. \tag{9}$$

The dimensionless energy

$$p_k=A_k^2/E, \tag{10}$$

measures the relative amount of energy which is stored in each topo–chrono pair and is a useful quantity for comparing different data sets. It has the properties of a probability distribution

$$0\leqslant p_k\leqslant 1 \quad \text{and} \quad \sum_{k=1}^{K}p_k=1. \tag{11}$$

In this context we also introduce the normalized entropy of the signal, defined as the entropy normalized to its maximum possible value

$$H=\frac{-\Sigma_{k=1}^{K}p_k\log p_k}{\log K}. \tag{12}$$

This parameter measures the degree of space–time complexity. It is equal to zero if and only if the signal is separable, i.e., when $y(x,t)=y(x)u(t)$. The maximum value $H=1$ is reached when all the components have equal weights.

Several statistical tests based on the weight or on the dimensionless energy distribution allow the assessment of the number of significant components for a given data set (see for example Refs. 10 and 23). We shall follow here a more qualitative approach having in mind the application to experimental plasma signals. Figure 1 illustrates a typical weight distribution and reveals some characteristic features. It shows a strong ordering with at least three significant components, representing together 99.7% of the signal energy. As a consequence, most of the signal features are contained in the three dominant topo–chrono pairs. This is further suggested by the small global entropy which is equal to $H=0.08$. It is legitimate to ask whether the remaining components may still contain pertinent information. The answer is usually negative because of the omnipresence of signal noise. To show this we consider a deterministic signal $\bar{y}(x,t)$ and add noise to it

$$y(x,t)=\bar{y}(x,t)+\eta(x,t). \tag{13}$$

The noise sequence $\eta(x,t)$ is defined here as a random fluctuation which is neither correlated in time nor in space. Its distribution is taken to be normal $N(0,\sigma^2)$. Note that the zero mean and the variance σ^2 apply both to time and space averages. It is reasonable to assume that the noise and the signal are uncorrelated. When N and M tend to infinity, the scatter matrices become

$$\mathsf{S}_x=\bar{\mathsf{S}}_x+N\sigma^2\mathsf{I}, \tag{14}$$

$$\mathsf{S}_t=\bar{\mathsf{S}}_t+M\sigma^2\mathsf{I}, \tag{15}$$

where I denotes identity matrices. The presence of noise only appears in the diagonal of the scatter matrices and thus merely shifts their eigenvalues by a value which is proportional to σ^2. The weights of the noisy signal become

$$A_k^2=\bar{A}_k^2+L\sigma^2, \tag{16}$$

where L is the largest of N and M. This expression shows a tendency of the high-order weights to converge toward a constant value regardless of the true distribution of the signal. Components whose weight exceeds $\sigma\sqrt{L}$ are well separated from the noise and reflect the characteristics of the signal whereas components associated with small weights are noise dominated. The presence of noise therefore sets an upper bound to the number of significant components that can be reasonably extracted from an experimental signal. In practice, the signal-to-noise ratio is rarely known *a priori* and the upper bound is found by locating the transition from a steep to a flat weight distribution. More realistic conditions such as non-Gaussian noise or finite data sets tend to smoothen the weight distribution and transform its flat tail into a gentle slope. For this reason the number of significant components cannot always be determined unambiguously; in Fig. 1 for example, this number may vary from 3 to 5 depending on the criteria used. Some criteria for locating the onset of noise are given in Refs. 23 and 24. Once the significant components are identified, they can be used to reconstitute the signal, thereby leaving out a significant fraction of the noise.

Another interesting property of the weight distribution shown in Fig. 1 is the presence of two identical and non-negligible weights $A_2=A_3$. This implies the presence of a degeneracy in the spectrum of the correlation function and can generally be ascribed to the existence of a spatiotemporal symmetry in the signal.[21] To illustrate this, we consider a sinusoidal traveling wave

$$y(x,t)=\alpha\cos(\omega t-kx), \tag{17}$$

which has the spatiotemporal symmetry

$$y(x,t+t_0)=y(x-x_0,t). \tag{18}$$

In the case where $N\omega\Delta t\gg 1$ and $Mk\Delta x\gg 1$ (Δt and Δx are, respectively, the average sampling period and the average spacing of the channels) the temporal and spatial scatter matrices of the sampled signal are

$$(S_x)_{ij}=\tfrac{1}{2}N\alpha^2\cos k(x_i-x_j), \tag{19}$$

$$(S_t)_{ij}=\tfrac{1}{2}M\alpha^2\cos \omega(t_i-t_j). \tag{20}$$

These rank 2 matrices only have two nonzero eigenvalues which are equal. In spite of an apparent arbitrariness in the definition of the eigenvectors, the topo–chrono pairs can be calculated unambiguously using the isomorphism (6). The weights are

$$A_k=\begin{cases}\dfrac{\alpha\sqrt{NM}}{2}, & k=1,2,\\ 0, & k>2,\end{cases} \tag{21}$$

and the corresponding topos and chronos are

$$\varphi_1(x_j)=\sqrt{2/M}\,\sin(kx_j), \tag{22}$$

$$\varphi_2(x_j)=\sqrt{2/M}\,\cos(kx_j), \tag{23}$$

$$\psi_1(t_i)=\sqrt{2/N}\,\sin(\omega t_i), \tag{24}$$

$$\psi_2(t_i)=\sqrt{2/N}\,\cos(\omega t_i). \tag{25}$$

In this particular case the biorthogonal components of the data matrix Y are identical to its discrete Fourier components. This is not true anymore when several traveling waves are superimposed. Waves with different frequencies or different wave numbers appear as distinct pairs of biorthogonal components, each pair having two equal weights. The Fourier transform generally does not allow a superposition of traveling waves to be identified unambiguously,[25] since it associates different wave numbers with each frequency. Such a reconstruction is made possible, however, when using the BD, using the procedure discussed in Ref. 12. It must be noted that waves with identical frequencies but different wave vectors (or alternatively identical wave vectors but different frequencies) are not separated and appear as a single pair of biorthogonal components. Different examples based on numerical simulations are given in Ref. 20. The mixing of different traveling waves into a single pair of biorthogonal components does not impede their reconstruction as long as the wave vectors (or, respectively, the frequencies) are sufficiently different.

In the more realistic case of traveling waves with slowly varying parameters, the topos and chronos merely reproduce the variations of the signal. For example, a temporal modification in the frequency $\omega/2\pi$ will appear in the chrono only but not in the topo. This property is particularly relevant for the analysis of transients and wavelets.

These examples reveal some of the properties of the BD that allow one to quickly recognize particular features in an experimental signal. Although the method is very general and needs few assumptions, it has the drawback of not being scaling invariant. It is easy to see that the biorthogonal components are sensitive to the scaling of the data. This effect has not been thoroughly investigated yet and the preprocessing of the data usually varies according to the nature of the experiment. A reasonable choice is to subtract the signal time average and normalize each channel by its standard deviation. If no background subtraction is made, the first component will just be the background itself and have an unusually large weight. A more appropriate normalization consists in dividing each signal channel by its noise level. This allows us to apply Eq. (16) and usually provides the clearest separation between significant and nonsignificant components. Another shortcoming of the BD is the difficulty to assign confidence intervals to its components. This difficulty can be ascribed to the high nonlinearity of the eigenvalue problems (4) and (5). A few results such as the asymptotic distribution of the weights for normal data can be found in the literature (see, for example, Ref. 10) but most statistical properties of the BD remain to be derived.

The BD can in principle be computed by solving the smallest of the eigensystems (4) and (5) together with Eq. (6). This approach, however, is subject to numerical stability problems and a more robust algorithm based on the SVD is preferred. This algorithm[26] yields directly the topos, the chronos, and the weights and requires approximately $(NM)^{3/2}$ operations. Its computational burden becomes significant when large data sets (typically $NM>10^5$) have to be analyzed but this problem can often be overcome by decomposing the data into smaller subsets and analyzing each of these separately.

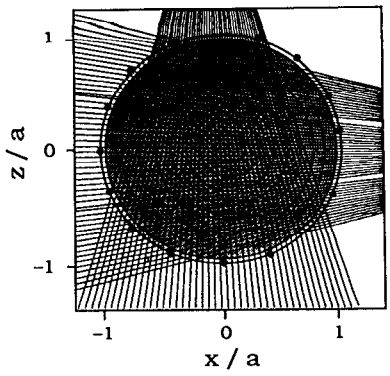

FIG. 2. Poloidal cross section of the Tore Supra tokamak showing the position of the plasma and the lines of sight of the two soft x-ray cameras. The dots indicate the position of the Mirnov coils; the high toroidal field side is to the left.

IV. APPLICATION TO SOFT X-RAY EMISSION FLUCTUATIONS

The soft x-ray emission of plasmas is often measured with high spatial and temporal resolution, which makes it a good candidate for a space–time analysis. The experiments to be described were carried out on Tore Supra, which is a circular cross-section tokamak with a minor radius $a=0.78$ m and a major radius $R=2.36$ m. The soft x-ray emission is measured by two pinhole cameras (one vertical, one horizontal, with, respectively, 44 and 53 detectors each, see Fig. 2)

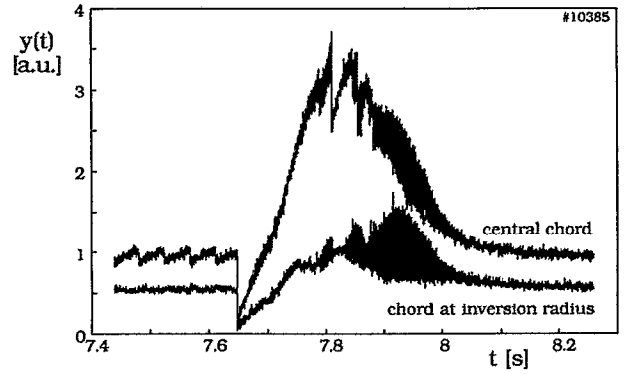

FIG. 3. Line-integrated soft x-ray emission measured along a central chord and a chord tangential to the sawtooth inversion radius. A deeply penetrating pellet is injected at $t=7.65$ s.

with a minimum time resolution of 1 μs. Local emission profiles are recovered using a projection on Zernicke polynomials, which is discussed in Ref. 27.

The soft x-ray emission is mostly sensitive to the electron density and temperature and is for that reason frequently used to monitor macroscopic MHD activity. Instabilities such as internal disruptions (or sawteeth) or single MHD modes are in general easily separated unless they occur simultaneously, in which case their identification becomes cumbersome. This situation is exemplified by a discharge in which a deeply penetrating deuterium pellet is injected, see Fig. 3. The cooling of the pellet first causes the soft x-ray emission profile to collapse but a peaked profile is recovered by applying 3 MW of ion cyclotron heating at the center of the plasma. After a 1/2 s sawteeth reappear, followed by strong MHD oscillations which degrade the energy confinement of the plasma. This discharge is described in more detail in Ref. 28.

The different phenomena that appear in Fig. 3 are difficult to disentangle and can only be identified after a careful and lengthy analysis of tomographic reconstructions. A Fourier analysis is not appropriate here since the signal is dominated by incoherent oscillations. The BD was applied to the line-integrated emission after subtracting the stationary level measured prior to the pellet injection; $N=2000$ time slices

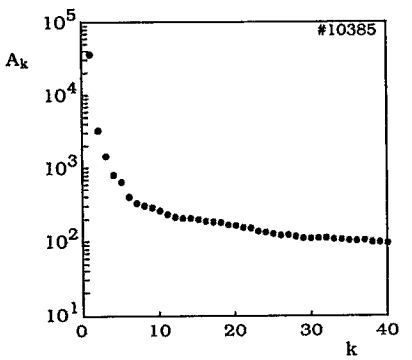

FIG. 4. Weight distribution calculated from the perturbed soft x-ray emission, with $N=2000$ time slices and $M=97$ channels. Only the 40 largest weights are displayed.

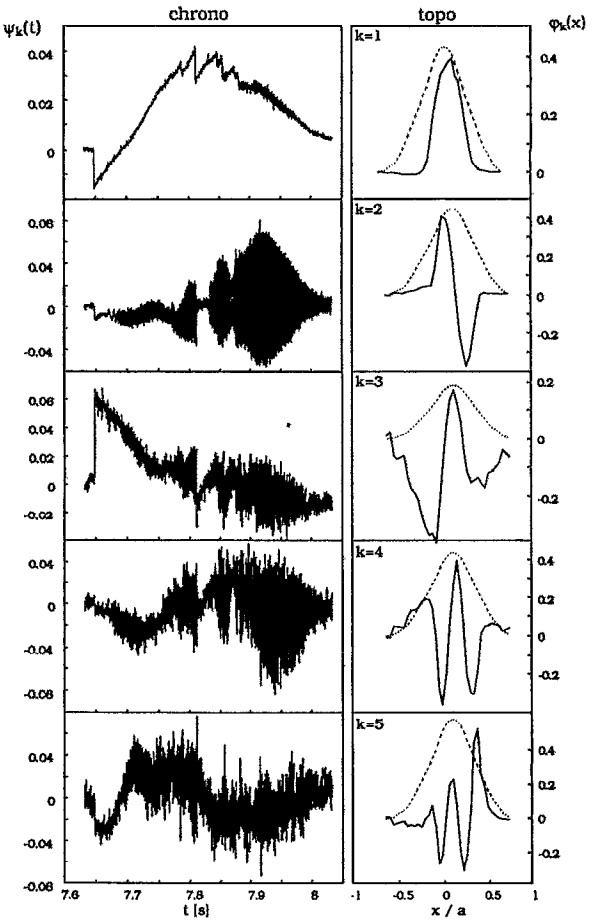

FIG. 5. The five dominant chronos and topos of the perturbed soft x-ray emission. Only topos of the vertical camera are displayed. Their spatial coordinate is defined as the intersection of the chords with the equatorial midplane. The stationary emission profile is shown for comparison with a dashed line and in arbitrary units.

and $M=97$ channels were used. The resulting weight distribution is shown in Fig. 4 and reveals approximately five significant components containing together 99.92% of the signal energy. A large redundancy in the data is attested to by the narrowness of the distribution. In this case, almost all the pertinent information contained in the signals can be reconstituted using less than 7% of the initial amount of data.

The five dominant topo–chrono pairs of the line-integrated soft x-ray emission are displayed in Fig. 5. Only the topos of the vertical camera are shown, using a spatial coordinate which is defined as the intersection of the chords with the equatorial midplane of the tokamak. The profile of the first topo is similar to that of the stationary emission although it has a stronger peaking which reflects the central temperature increase. Given its shape, we expect its corresponding chrono to be sensitive to sawtooth crashes. Sawteeth are indeed apparent in the first chrono, which displays them much better than any of the raw signals. The second biorthogonal component, on the contrary, shows no sawteeth but fast fluctuations. Its topo is radially asymmetric and a tomographic reconstruction shown in Fig. 6 clearly reveals a dipole structure. It is usual to characterize such structures by

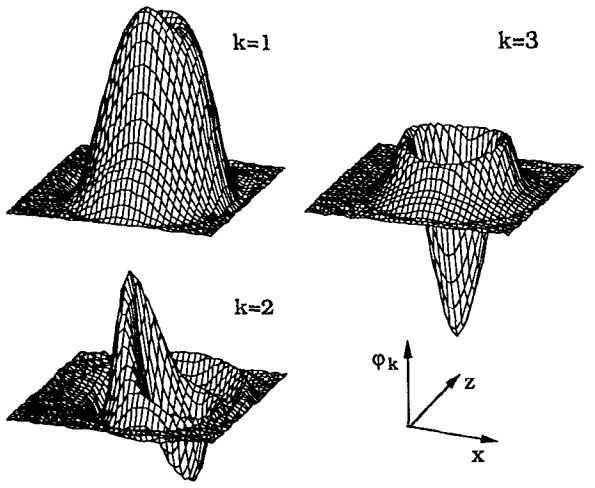

FIG. 6. Perspective plot of the reconstructed topos of the perturbed soft x-ray emission, showing the annular structure associated with the $m=0$ topology of the sawteeth (topos 1 and 3) and the $m=1$ topology of the rotating mode (topo 2). Only the central part of the plasma is displayed ($-0.5<x/a<0.5$ and $-0.5<z/a<0.5$) and the view is taken from a position below and outside of the chamber. The small peripheral annular structures are an artifact of the tomographic reconstruction procedure.

approximating them by a Fourier decomposition in cylindrical geometry, using the poloidal (θ) and toroidal (ϕ) angles

$$\varphi(r,\theta,\phi,t)=\varphi_{nm}(r)\exp[j(\omega_{nm}t-n\phi-m\theta)]. \quad (26)$$

The absence of toroidal resolution prohibits an assessment of the toroidal topology but poloidal mode numbers up to $m=2$ can be resolved with the two cameras. The rotating dipole is identified as an $m=1$ mode located near the sawtooth inversion radius. We already conclude that the BD has separated the dynamics of the sawteeth (whose dominant mode number is $m=0$) from the rotation of the $m=1$ mode. Figure 7 shows how the mode rotation frequency and amplitude are affected by each sawtooth crash. The third topo–chrono pair is again radially symmetric and thus mostly sensitive to the sawteeth. Some cross-talk with the $m=1$ mode can be observed, indicating that the BD does not fully separate the two effects. Furthermore, a slight departure from a purely symmetric radial profile must be noticed. This is ascribed to the outward shift of the plasma flux surfaces, which is induced by the central heating and causes the emission profile to lean outwards. The fourth topo is asymmetric and its chrono mainly displays the first harmonic of the rotation frequency. Higher-order components have more complex topos and are increasingly affected by noise. The sixth component is about the largest which still reveals some macroscopic structures and marks the onset of noise, as could be expected from the break in the weight distribution.

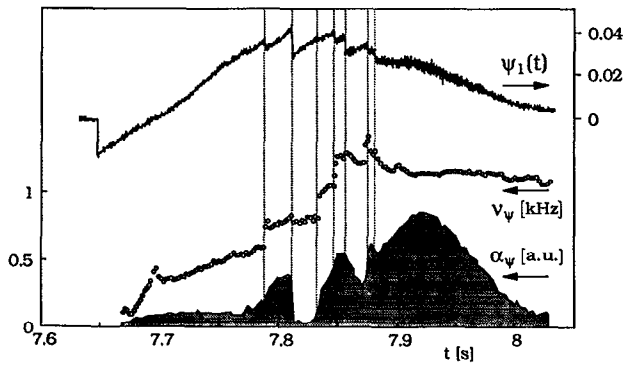

FIG. 7. Time evolution of the $m=1$ mode rotation frequency and amplitude. The first chrono is displayed for comparison and shows how each sawtooth affects the rotation.

The BD appears here as a powerful tool for separating the features associated with different physical mechanisms on the basis of their spatial and temporal structures. An important result is the possibility to reduce large data sets into small numbers of deterministic components that can be meaningfully compared. In this sense the BD allows existing results to be improved or at least to be illustrated in a more straightforward way. A typical example is the $m=1$ oscillation, which would have been more difficult to resolve by other means. An equally important result is the high reproducibility of the topos whose shape hardly changes if the BD is applied to shorter time windows. This strongly suggests that the different aspects of the observed dynamics are all described by a common and well-defined mechanism. This aspect will be further examined in Sec. VI.

Although the nomenclature of the BD explicitly refers to spatiotemporal signals, the method can be applied to any kind of bivariate signal. It is most appropriate when the data contains redundancies as the salient features are then captured by few modes. The BD of a set of totally uncorrelated data results in equally weighted components and no pertinent information can be gained in that case. In practice, the minimum size a data matrix should have depends on the amount of collinearity between the data; in many cases, significant results can already be obtained with sizes as small as $K=4$. We also point out that some features may be left unnoticed because they do not clearly appear in one particular component. Perturbations that are not separable such as radial expansions or horizontal displacements of the emission profile cannot be expressed by a single topo–chrono pair and thus appear in several components. For this reason it may occasionally be necessary to repeat the BD for shorter time or space intervals in order to visualize a local change in the components.

A different example of feature extraction is provided by the biorthogonal decomposition of the soft x-ray response to an injection of impurities. Figure 8 shows the emission measured along two chords during an Ohmic discharge in which a small amount of nickel was injected. Laser-ablated impurity injection has become a standard method for studying impurity transport[29] and furthermore provides some insight into internal MHD instabilities.[30] The temporal evolution of two line-integrated measurements depicted in Fig. 8 suggests the presence of an inverted sawtooth crash occurring shortly after the injection but does not give full evidence of it. Such inverted crashes are caused by a rapid impurity influx toward the center of the plasma.

The BD was applied to the perturbed line-integrated emission with the aim to separate concurrent effects such as

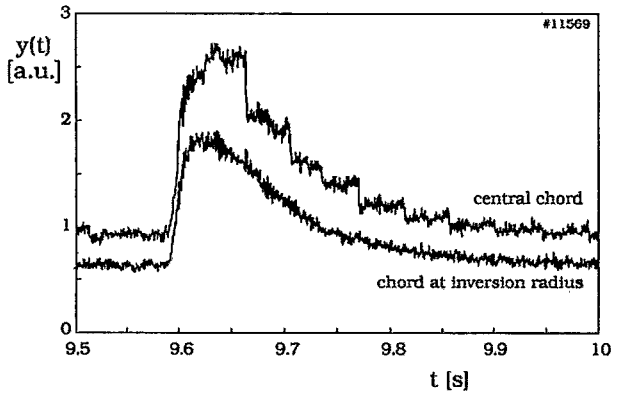

FIG. 8. Line-integrated soft x-ray emission measured along a central chord and a chord tangential to the sawtooth inversion radius. Impurities are injected at $t=9.58$ s.

the sawteeth and the perturbation caused by the impurity injection. Figure 9 shows the weight distribution as obtained from the vertical camera and suggests the existence of four significant components. The latter are plotted in Fig. 10 together with the stationary emission profile. The first topo is just proportional to the stationary profile and reflects the global increase in emissivity due to the higher concentration of impurities. It is similar to the first topo of the previous example, though not as peaked and asymmetric because no significant outward shift of the plasma flux surfaces occurs during this experiment. The second and third topo represent more complex radial structures which show an increasing number of nodes. The second chrono is particularly sensitive to sawteeth and clearly reveals the expected inverted sawtooth crash 20 ms after the injection time. Again, such a feature is much better observed in the biorthogonal components than it could be in the raw signals. An unsuspected result is the presence of a rotating $m=1$ mode which appears in the fourth component. It is well observed between subsequent sawtooth crashes and also appears shortly during the crashes. The larger mode amplitude observed after the injection has already been reported[30] and mainly results from the global emission enhancement caused by the larger concentration of impurities. The apparent disappearance of the

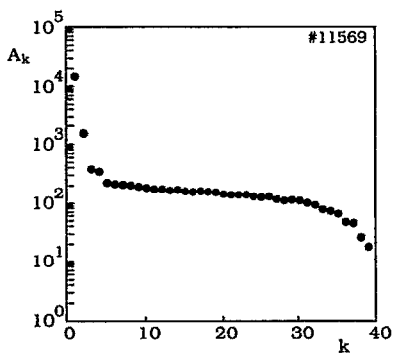

FIG. 9. Weight distribution of the perturbed soft x-ray emission in the case of impurity injection, with $N=2000$ time slices and $M=39$ channels. Only components of the vertical camera are considered.

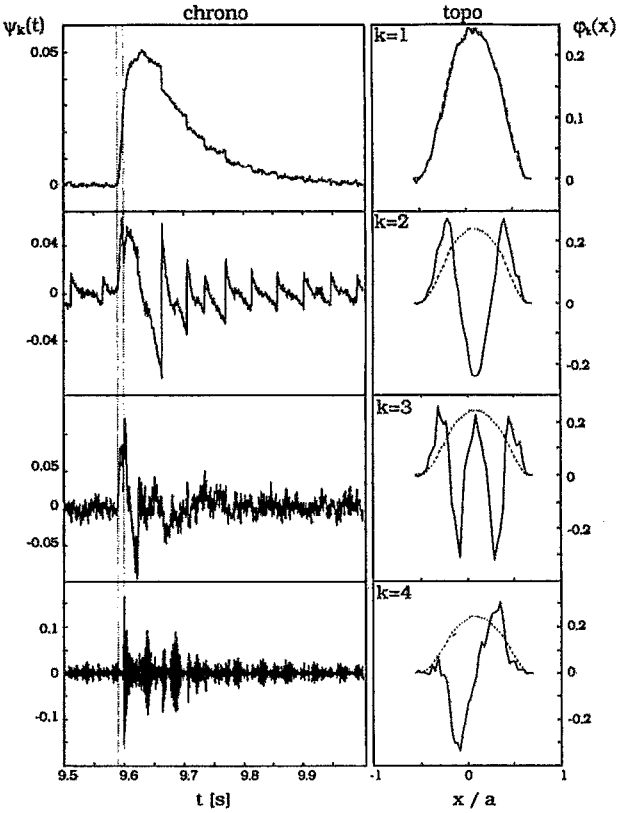

FIG. 10. The four significant components of the perturbed and line-integrated soft x-ray emission during an impurity injection. Only topos from the vertical camera are displayed, together with the stationary emission profile (dashed line, arbitrary units).

mode between the injection of the impurities and the inverted sawtooth is due to the hollowness of the emission profile at that time, which prevents the central emission from being well resolved.

V. APPLICATION TO MAGNETIC FIELD FLUCTUATIONS

A different example of spatiotemporal dynamics is provided by the magnetic field fluctuations that are measured outside a plasma. Such fluctuations are generally dominated by coherent oscillations which are generated by the rotation of magnetic islands inside the plasma. The poloidal component of the fluctuating magnetic field is measured in Tore Supra by arrays of Mirnov coils located at different poloidal and toroidal angles. The signals are low-pass filtered with a cutoff frequency at 12 kHz and subsequently sampled at 32 kHz. We consider here a single array of 14 coils located in the same poloidal plane, see Fig. 2.

Coherent oscillations of the magnetic field are usually identified by performing a Fourier transform on the signals and subsequently analyzing the poloidal or toroidal dependence of the calculated phases for each of the dominant frequencies.[31] This procedure is straightforward when the frequencies vary little in time but does not readily apply to transients. In the latter case, the spectra must be computed for short time intervals, which is statistically unfavorable. An

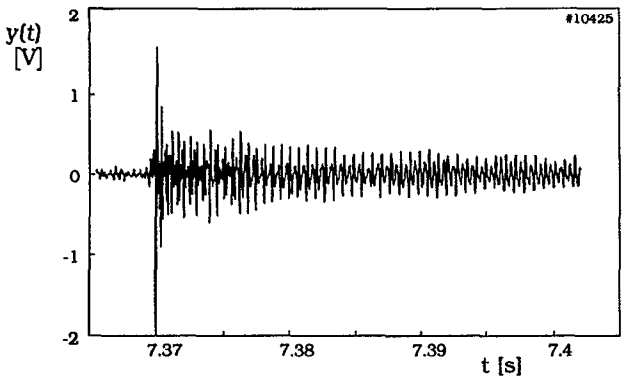

FIG. 11. A Mirnov coil signal showing the burst of MHD activity which is triggered by the crash of a monster sawtooth.

example of transient MHD activity is provided by a discharge in which a monster sawtooth crash occurred. Monster sawteeth lasting for about 800 ms have been produced in Tore Supra by the combined application of lower-hybrid current drive and ion cyclotron heating.[32] Each crash generates a strong burst of MHD activity, one of which is illustrated in Fig. 11. This sequence was analyzed with $N=1140$ time slices and $M=14$ signals, after normalizing each coil signal to its standard deviation. The weight distribution, which is represented in Fig. 12, shows at least two pairs of values which are close enough to suggest the existence of spatiotemporal symmetries. Coherent oscillations are clearly observed in the six dominant chronos, which contain together 97% of the signal energy, see Fig. 13. The corresponding topos are displayed for convenience in polar coordinates, in which the angular position is that of the coils and the radial coordinate the amplitude of the topo.

From the discussion in Sec. III, it is clear that the six most significant components represent three rotating modes. Each mode consists of two oscillating topo–chrono pairs which are in quadrature (i.e., both topos and chronos are phase shifted by $\pi/2$). This separation into different frequency components is made apparent by the frequency power spectral density of the chronos, shown in Fig. 14. For a given time interval, the spectrum of the six dominant chronos is narrow and dominated by a single frequency whereas higher-order terms have a broader spectrum. Three dominant frequencies can be identified, each of which appears in a different pair of components. The poloidal mode numbers of the topos can be inferred from the number of lobes which are observed in the polar representation and are, respectively,

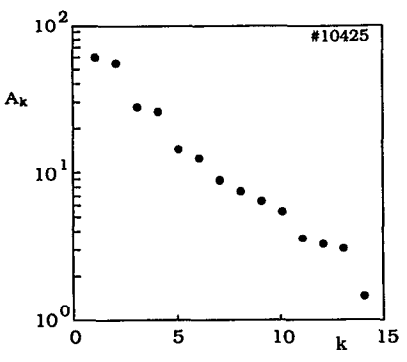

FIG. 12. Weight distribution calculated from the Mirnov coil measurements during a monster sawtooth, with $N=1141$ time slices and $M=14$ channels. At least two pairs of similar weights can be distinguished.

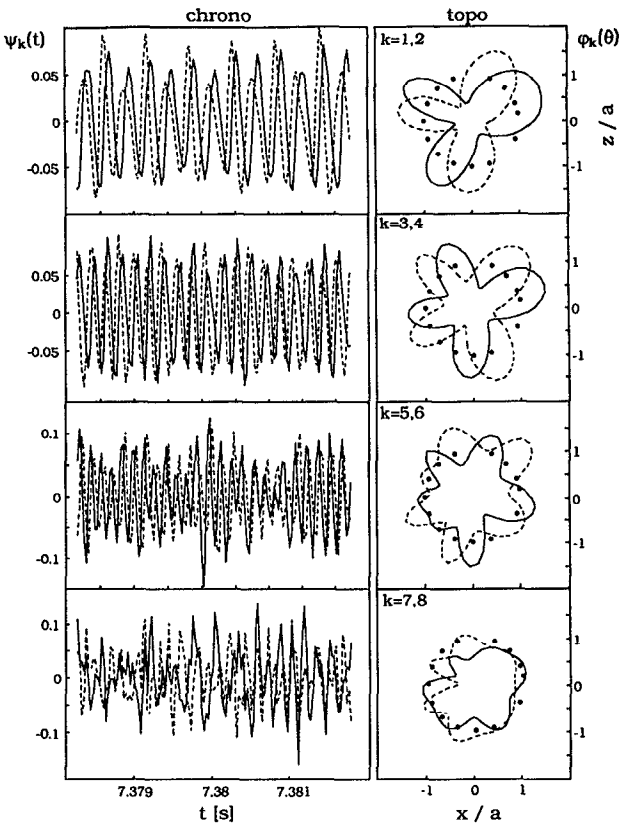

FIG. 13. Eight dominant topos and chronos of the magnetic field measurements displayed for a short time interval. The solid lines represent odd numbered components and the dashed lines even ones. Polar coordinates are used for the topos whose amplitude is normalized between 0.5 and 1.5. The positions of the Mirnov coils are indicated by dots.

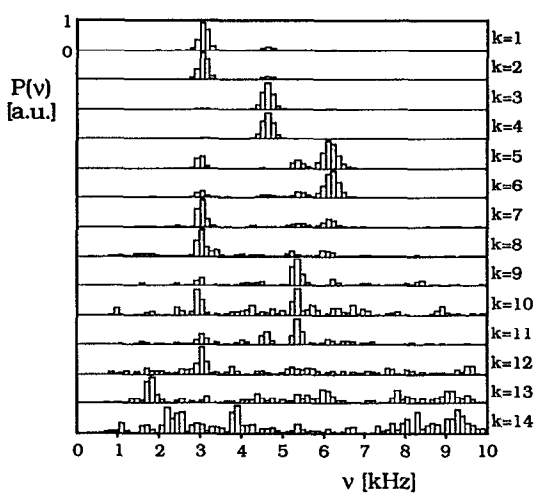

FIG. 14. Power spectral density of the 14 chronos shown in Fig. 13.

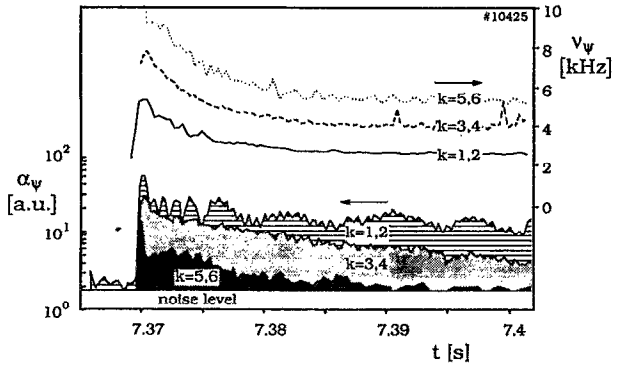

FIG. 15. Time evolution of the amplitude and the angular frequency of the modes that are generated by the crash of the monster sawtooth. No particular mode activity is observed before the crash. Note the good time resolution of the mode parameters.

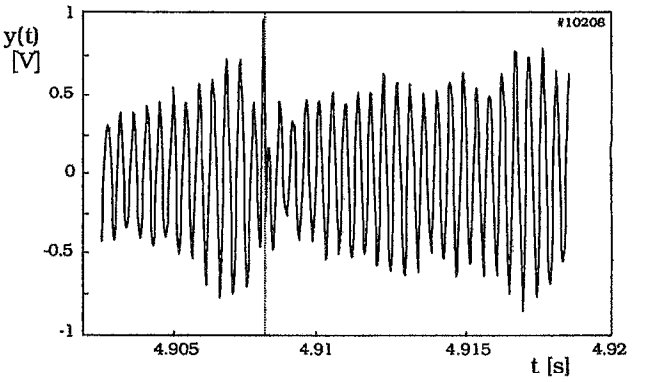

FIG. 16. Raw Mirnov coil signal showing mode activity and a discontinuity caused by a sawtooth crash.

$m=3$, 4, and 6. The higher concentration of lobes near the high toroidal magnetic field side is a well-known effect which is due to the toroidal geometry and to the off-center position of the mode with respect to the coil array.[33]

Toroidal mode numbers can be obtained in a similar way by extending the analysis to Mirnov coils located at different toroidal angles. We finally identify three dominant MHD modes whose topologies are, respectively, $(n,m)=(2,3)$, (3,4) and (4,6), in agreement with results obtained using a standard Fourier analysis. The poloidal mode number $m=6$ is about the largest we can identify, given the finite angular resolution of the Mirnov coil array. The presence of other modes with different frequencies or topologies is not excluded but their amplitude is too small for them to be identified. Their existence is suggested by the power spectrum shown in Fig. 14. It is also supported by the weight distribution which, unlike that of the soft x-ray emission, does not flatten at high values of k. As a consequence, not one of the 14 biorthogonal components is fully noise dominated and each one contains pertinent information about the magnetic field fluctuations.

Other parameters of the fluctuating signal can be calculated by analogy with the example treated in Sec. III. The angular frequency and the amplitude associated with the three dominant pairs of components are

$$\nu(t_i)=\frac{1}{2\pi}\left|\frac{d}{dt}\left(A\tan\frac{\psi_k(t_i)}{\psi_{k+1}(t_i)}\right)\right|, \quad k=1,3,5, \tag{27}$$

$$\alpha(t_i)=\sqrt{\psi_k^2(t_i)+\psi_{k+1}^2(t_i)}, \quad k=1,3,5. \tag{28}$$

The time evolution of these parameters is shown in Fig. 15. No precursor is observed prior to the sawtooth crash, which is followed by a rapid slowing down of the rotation. From this figure, the damping rates of the different modes can be calculated with an excellent time resolution.

It has been early recognized that magnetic islands tend to rotate only in the toroidal direction, with the same toroidal angular velocity.[34] This is supported by our results since the ratio between the angular frequency ν and the toroidal mode number n is exactly the same for the three dominant modes. Nevertheless, the possibility for islands to rotate in the poloidal direction or with different toroidal angular velocities cannot be completely ruled out. As pointed out in Ref. 12, the presence of more than one frequency component in the power spectrum of the chronos is generally an indication that the corresponding traveling waves propagate at different velocities. Such multiple frequencies are apparent in the power spectra of the high-order chronos shown in Fig. 14, and can also be observed in the dominant ones. Similar conclusions can in principle be drawn from the power spectral density of the topos, in which the presence of more than one mode number is also an indication of differing velocities. In our case, however, no assessment of the spectrum of the topos can be made since this would require a detailed knowledge of the distortions caused by the toroidal geometry. The spectrum of the chronos will be discussed in future work.

This example shows how different rotating modes can be separated by the BD without knowing *a priori* their frequency or the number of modes present. In contrast to spectral techniques, these modes are distinguished on the basis of their poloidal structure, which is invariant, and not on frequency considerations, which may evolve in time. A major improvement over a standard Fourier analysis is the absence of constraints on the time resolution, which can be freely chosen. This property allows us to resolve very short and transient phenomena. It can be used, for example, to confirm the constancy of the toroidal velocity ratio between the different modes immediately after the sawtooth crash.

A different aspect of the BD is illustrated by the following example, in which we consider the MHD activity which occurs during a normal sawtooth crash. The signals were recorded during an Ohmic discharge, in which some MHD activity was triggered by an injection of gas. The sequence which was analyzed shows a strong oscillation with a discontinuity caused by the sawtooth crash, see Fig. 16. The weight distribution and the dominant biorthogonal components corresponding to this sequence are shown in Figs. 17 and 18. We identify a strong $m=2$ oscillation in the first two terms, and a barely perceptible $m=4$ mode in the fourth and fifth ones. The third biorthogonal component does not have the properties of a traveling wave and reveals a short perturbation. It is interpreted as a gong mode[35] which is caused by the sawtooth crash occurring at that time inside the plasma.

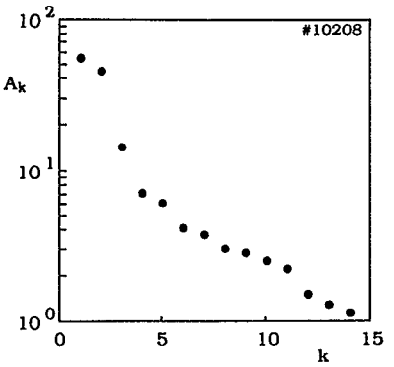

FIG. 17. Weight distribution of the magnetic field measurements during a normal sawtooth, with $N=400$ time slices and $M=14$ channels.

This mode propagates in the poloidal and toroidal directions like the other modes but its duration is shorter than its rotation period. This explains why it appears in a single biorthogonal component rather than two. In spite of its short lifetime, the poloidal topology of the gong is well resolved and the mode number is $m=3$. In JET, the dominant mode number of the gong was found to be equal to the integer part of the safety factor $q_\psi(a)$, as measured at the last closed flux surface.[35] In our case $q_\psi(a)=3.4$ and the agreement is good. It must be noted that the $m=2$ mode shows no significant discontinuities during the sawtooth crash.

We conclude from this example that the gong mode can be directly identified from the biorthogonal components. The BD has also been applied to other discharges and so far the mode numbers agree with the empirical predictions for safety factors in excess of 3. A surprising result, however, is

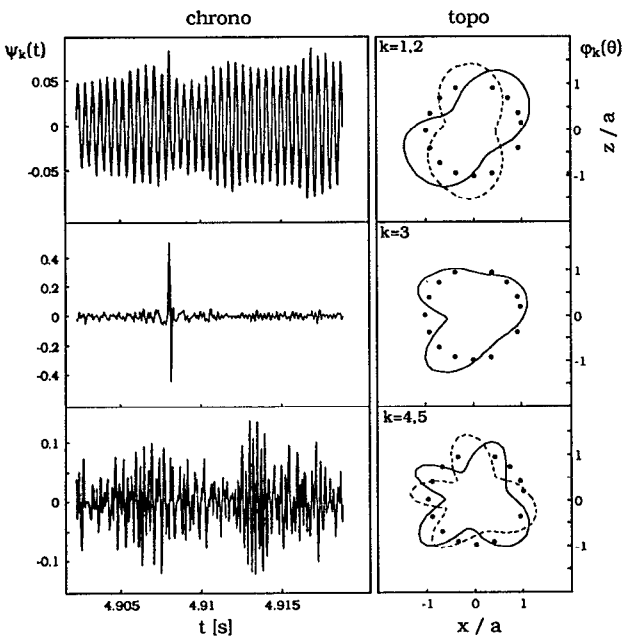

FIG. 18. Five dominant topos and chronos of the magnetic field measurements. The chronos 2 and 5 are not displayed since they are merely in quadrature with the chronos 1 and 4. The gong mode clearly appears in the third biorthogonal component.

the observation of dominant $m=3$ mode structures for discharges whose safety factor drops below 3, down to 2.4. We finally point out that the separation of contending perturbations is possible provided that their poloidal mode numbers differ. If the poloidal topology of the gong had been identical to that of the $m=2$ mode, both would have appeared together in a single pair of biorthogonal components. In that case, however, the gong could still be recognized by a short burst in the chrono.

VI. DISCUSSION AND OUTLOOKS

The results that have been presented so far bear many similarities with those obtained in JET using the SVD[20] and we recall that both approaches are formally identical. The framework of the BD, however, has been preferred to that of the SVD because this kind of analysis is not restricted to linear or stationary processes. Although the BD is essentially based on second-order moments of the data, it can be used as well to investigate nonlinear phenomena. Its ability to identify macroscopic structures in fluctuating signals leads us to briefly discuss here a particularly relevant application, which is the search for organized behavior in plasma turbulence.

The role played by coherent vortex structures in plasma transport processes has become an important research issue in the last decades. Numerical simulations[36,37] and experiments[38–40] both lend support to their existence but most results have remained qualitative and inconclusive so far due to a lack of adequate analysis techniques. A major problem is the objective quantification of the degree of organization in a turbulent regime. Although coherent structures are generally easy to visualize in spatiotemporal signals, it is much more difficult to formulate a test statistic capable of identifying and extracting them.[41] Such a test statistic must be data adaptive if it is to detect coherent structures without *a priori* knowledge of their shape or location. The BD possesses such data-adaptive properties, which makes it a useful complement to usual correlation and conditional averaging techniques.

Although the application of the BD to the characterization of complex spatiotemporal dynamics has been advocated by several authors (see for example Refs. 42 and 43), the method has only recently been used in plasma physics. The first known application to plasma turbulence[44] reports the analysis of spatiotemporal density fluctuation measurements in the scrape-off layer of the ASDEX and ADITYA[16] tokamaks. In these experiments, the existence of coherent structures in regimes of fully developed turbulence is clearly revealed by the BD. The method allows one to extract these structures, which can thereafter be characterized with statistical tools. Such preliminary results are encouraging and suggest that substantial progress can still be achieved in the analysis of spatiotemporal turbulence.

An issue which has not been discussed yet is the physical interpretation of the biorthogonal components. Indeed, techniques such as the BD and the principal component analysis are often criticized for the difficulty to interpret their components in physical terms. This criticism is generally justified when the data matrix contains a mixture of different physical quantities. However, when the data set represents a

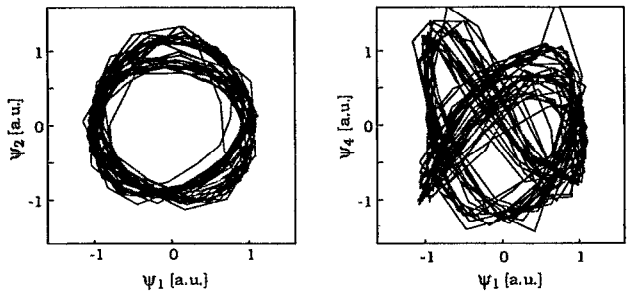

FIG. 19. Orbit representation of the chrono pairs (ψ_1,ψ_2) and (ψ_1,ψ_4), revealing Lissajou figures. The chronos of Fig. 13, measured after a monster sawtooth, have been used.

single quantity, like in the preceding examples, a physical interpretation is often apparent. An early effort to provide a physical interpretation was made in meteorology where close links were found between principal components of pressure fields and eigensolutions of the differential equations that describe the dynamics of the atmosphere.[23]

Among the different kinds of fluctuating signals that have been considered here, the soft x-ray emission has components that can be easily interpreted. The analogy, which is further discussed in the Appendix, reveals a strong link between the radially symmetric topos and the eigensolutions of the plasma particle and heat transport operators. A characteristic signature of this analogy is the number of nodes in the topos, which increases with the order k. This analogy with spectral properties of transport operators also provides an explanation for the limited number of components that is needed to adequately reproduce the dynamics of the perturbed soft x-ray emission.

An analogy may also be made between the decomposition of the magnetic field fluctuations and that of embedded time series.[22] To this end, we consider the chronos presented in the first part of Sec. V and use orbit representations, see Fig. 19. The orbits described by the pairs (ψ_1,ψ_2), (ψ_3,ψ_4) and (ψ_5,ψ_6) are circular, which simply expresses the fact that the chronos oscillate in quadrature and at a single frequency. The orbits involving chronos from different pairs indicate whether these oscillate independently. The orbit of (ψ_1,ψ_4), for example, reveals a limit cycle. From the identification of its Lissajou figure we conclude that the frequency ratio between the $(n,m)=(3,4)$ and (2,3) modes is exactly 1.5. The presence of a Lissajou figure instead of a diffuse cloud gives a direct evidence of a mode locking, i.e., the modes rotate in phase as if the plasma were a rigid body. The same conclusion pertains to the (4,6) mode whose frequency is exactly twice that of the (2,3) mode. The orbit representation also applies to the chronos of the soft x-ray emission but the proper correspondence must be given in the interpretation. The orbit (ψ_2,ψ_4) is a partial Lissajou figure corresponding to the rotation of the $m=1$ island; the space spanned by (ψ_1,ψ_3) has a different meaning and can be interpreted in terms of the temporal evolution of the profile shape.

Finally, it must be mentioned that the BD is widely used in signal processing under the name SVD.[45] Among the applications that can be relevant to plasma physics experiments, we note the possibility to ease the reconstruction of local plasma parameters from line-integrated measurements. A major handicap common to most reconstruction techniques is the necessity to repeat them as many times as there are snapshots needed. This, however, can often be circumvented using the property of a reconstructed signal to be equal to its reconstructed biorthogonal components. In many cases, it is computationally much more advantageous to invert a few topos, which immediately provide access to the full time evolution, rather than inverting repetitively large numbers of profiles.

VII. CONCLUSION

The ability of the BD to disentangle complex spatiotemporal signals into coherent structures makes it a powerful tool for analyzing fluctuations in plasmas. The first reason is that it provides a full spatiotemporal description which splits the dynamics into spatial and temporal modes. Second, it concentrates the dominant dynamical features into a few number of modes only, thereby easing their interpretation.

A first application of the BD to soft x-ray measurements shows that the apparently complex behavior of the emission profile can be decomposed into simple and reproducible modes. Using the BD, contending phenomena such as sawteeth and MHD oscillations are clearly separated and therefore easier to examine. The structure of the spatial modes is found to be directly related to the properties of the particle and heat transport mechanisms. This explains the low dimensionality of the soft x-ray signals, which only need a few modes to be adequately modeled.

A second application to magnetic field fluctuations shows that different rotating MHD modes can be separated without knowing *a priori* their frequency or the number of modes present. A clear improvement over spectral techniques is obtained, owing to the fact that the BD treats both space and time dependences simultaneously. This allows, for example, the gong mode structure to be clearly identified. Finally, it is shown how the data must be preprocessed in order to overcome the undesirable effects that may be caused by the lack of scaling invariance of the method.

The BD has already been successfully applied in fluid mechanics to study the transition to turbulence. We believe that significant progress can be achieved in the understanding of plasma dynamics by using it with spatially resolved measurements, which are now becoming increasingly commonplace.

ACKNOWLEDGMENTS

We are indebted to the support of the Tore Supra team and acknowledge Sophie Turlur for carrying out a Fourier analysis of the magnetic signals. We also thank Dr. Xavier Garbet, Dr. Louis Laurent, and Dr. Yves Peysson for making useful comments on the manuscript.

The first author (T.D.) gratefully acknowledges support by the Commission of the European Communities under EURATOM Grant No. ERB 4001GT920020.

APPENDIX: ANALOGY WITH EIGENMODE REPRESENTATION

It is known in the context of perturbative transport analysis[46,47] that the linearized dynamical response of plasma parameters such as the electron density and temperature can be described in terms of spatial eigenmodes $f_k(x)$, each of which is characterized by a decay time τ_k. The Laplace transform of this expression reads

$$y(x,s)=\sum_{k\geq 1} f_k(x)\,\frac{\tau_k u(s)}{s\tau_k+1}, \tag{A1}$$

where $u(s)$ is the stimulus and s the Laplace variable. The inverse Laplace transform gives

$$y(x,t)=\sum_{k\geq 1} f_k(x) g_k(t). \tag{A2}$$

The spatial components $f_k(x)$ turn out to be eigenfunctions of the operator which governs the dynamical response, hence the name *eigenmode representation*. A direct physical interpretation can be assigned to these eigenfunctions which can either be calculated analytically from transport models or measured experimentally; in both cases the result is an infinite set of functions whose number of nodes increases with k.

The eigenmode decomposition (A2) is in many aspects similar to the BD since it also projects a spatiotemporal signal onto a set of separable functions. This similarity clearly appears in Fig. 20, which compares the spatial components obtained by the two decompositions for a simulated signal. A diffusive transport model in cylindrical geometry was used to build a spatiotemporal set of data which was subsequently decomposed in eigenfunctions and topos. The discrepancies seen in Fig. 20 are due to the properties of the modes, which satisfy different constraints. The temporal components $g_k(t)$ are not orthogonal as opposed to the chronos; furthermore, their structure is partly known *a priori*, whereas the chronos are not predefined.

Given the strong similarity between the BD and the eigenmode decomposition, we can attribute a physical meaning to the topos of the perturbed soft x-ray emission. The radially symmetric topos express the relaxation of the emission profile and their structure is a direct consequence of the diffusive nature of the underlying transport mechanisms. In Fig. 10, for example, the three most significant topos can be associated with the three lowest eigenmodes of the mechanism which governs the impurity transport. The radially asymmetric topos on the contrary represent processes which involve poloidal transport.

A consequence of this analogy is the small number of components that is needed to model the relaxation of the soft x-ray emission profile. This surprising property has also been observed in other quantities such as the electron density and has generally been ascribed to some intrinsic smoothness in the underlying physics. If we apply the eigenmode decomposition to such quantities, a rapidly decreasing series of decay times τ_k results. Only few of these time constants exceed the data acquisition period so that high-order eigenmodes cannot be resolved. As a consequence, most of the observed signal dynamics is confined to a few slow eigenmodes only (typically two to four) and accordingly, the number of significant components must be small. Phenomena which do not readily fit into this eigenmode representation generally require more biorthogonal components to be modeled. This is the case with the magnetic fluctuation data, for which at least ten components are found to be significant.

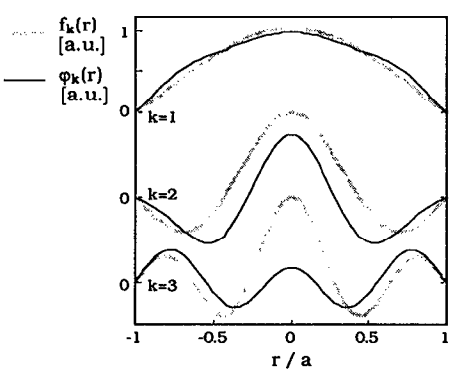

FIG. 20. Comparison between the radial eigenfunctions (gray line) and the topos (black line), as calculated from a simulated spatiotemporal signal in cylindrical geometry.

[1]Ch. P. Ritz, E. J. Powers, T. L. Rhodes, R. D. Bengston, K. W. Gentle, H. Lin, P. E. Philips, A. J. Wootton, D. L. Brower, N. C. Luhmann, Jr., W. A. Peebles, P. M. Schoch, and R. L. Hickok, Rev. Sci. Instrum **59**, 1739 (1988).

[2]J. D. Bell, J. H. Harris, J. L. Dunlap, N. A. Crocker, and V. K. Paré, Rev. Sci. Instrum. **64**, 2428 (1993).

[3]J. L. Lumley, *Stochastic Tools in Turbulence* (Academic, New York, 1970).

[4]B. J. Cantwell, Annu. Rev. Fluid Mech. **13**, 456 (1981).

[5]N. Aubry, P. Holmes, J. L. Lumley, and E. Stone, J. Fluid Mech. **192**, 115 (1988).

[6]L. Sirovich and M. Kirby, Phys. Fluids A **2**, 127 (1990).

[7]H. Wind, in *Formulae and Methods in Experimental Data Evaluation*, edited by R. K. Bock, K. Bos, S. Brandt, J. Myrheim, and M. Regler (European Physical Society, Geneva, 1984), Vol. 3, Paper K.

[8]P. A. Devijver and J. Kittler, *Pattern Recognition: A Statistical Approach* (Prentice–Hall, Englewood Cliffs, NJ, 1982), pp. 301–341.

[9]M. Loève, *Probability Theory*, 3rd ed. (Van Nostrand, Princeton, 1963), pp. 477–485.

[10]K. V. Mardia, J. T. Kent, and J. M. Bibby, *Multivariate Analysis* (Academic, London, 1979), pp. 213–254.

[11]G. H. Golub and C. F. Van Loan, *Matrix Computations*, 2nd ed. (The John Hopkins University Press, Baltimore, MD, 1989).

[12]N. Aubry, R. Guyonnet, and R. Lima, J. Stat. Phys. **64**, 683 (1991).

[13]N. Aubry, R. Guyonnet, and R. Lima, J. Nonlinear Sci. **2**, 183 (1992).

[14]N. Aubry, F. Carbone, R. Lima, and S. Slimani, "Wave propagation phenomena from a spatio-temporal viewpoint: Resonances and bifurcations, to be published in J. Stat. Phys.

[15]R. Lima, Chaos **2**, 315 (1992).

[16]For a general reference to fusion devices, see *World Survey of Activities in Controlled Fusion Research* (International Atomic Energy Agency, Vienna, 1991) [Nucl. Fusion special supplement (1991)].

[17]B. J. Braams, W. Jilge, and K. Lackner, Nucl. Fusion **26**, 699 (1986).

[18]B. Ph. van Milligen and N. J. Lopes Cardozo, Comp. Phys. Comm. **66**, 243 (1991).

[19]D. Brotherton-Ratcliffe, C. G. Gimblett, and I. H. Hutchinson, Plasma Phys. Controlled Fusion **29**, 161 (1987).

[20]C. Nardone, Plasma Phys. Controlled Fusion **34**, 1447 (1992).

[21]N. Aubry and R. Lima, "Spatio-temporal symmetries," submitted to J. Stat. Phys.

[22]D. S. Broomhead and G. P. King, Physica D **20**, 217 (1986).

[23]R. W. Preisendorfer, *Principal Component Analysis in Meteorology and Oceanography* (Elsevier, Amsterdam, 1988).
[24]T. Dudok de Wit, "Enhancement of multichannel data in plasma physics by biorthogonal decomposition," submitted to Plasma Phys. Controlled Fusion.
[25]W. I. Neuman, D. K. Campbell, and J. M. Hyman, Chaos **1**, 77 (1991).
[26]W. H. Press, B. P. Flannery, S. A. Teukolsky, and W. T. Vetterling, *Numerical Recipes, the Art of Scientific Computing* (Cambridge University Press, Cambridge, 1988), pp. 60–71.
[27]R. S. Granetz and P. Smeulders, Nucl. Fusion **28**, 457 (1988).
[28]A. Géraud, M. Chatelier, H. W. Drawin, C. Gil, B. Pégourié, A. L. Pecquet, Y. Peysson, J. M. Picchiottino, B. Saoutic, and C. Desgranges, in *Proceedings of the 20th European Conference on Controlled Fusion and Plasma Physics*, Lisboa, edited by J. A. Costa Cabral, M. E. Manso, F. M. Serra, and F. C. Schüller (European Physical Society, Geneva, 1993), Vol. 17C, Part I, p. 163.
[29]M. Shimada, Fusion Eng. Design **15**, 325 (1992).
[30]A. Compant La Fontaine, M. A. Dubois, A. L. Pecquet, D. Boyd, A. Cavallo, S. Cohen, S. Von Goeler, R. Hulse, D. Manos, R. Smith, and R. Wilson, Plasma Phys. Controlled Fusion **27**, 229 (1985).
[31]T. R. Harley, D. A. Buchenauer, J. W. Coonrod, and K. M. McGuire, Nucl. Fusion **29**, 771 (1989).
[32]D. Moreau, B. Saoutic, A. Agarici, B. Beaumont, A. Becoulet, G. Berger-By, P. Bibet, J. P. Bizarro, J. J. Capitain, J. Carrasco, T. Dudok de Wit, C. Gil, M. Goniche, R. Guirlet, G. Haste, G. T. Hoang, E. Joffrin, K. Kupfer, H. Kuus, J. Lasalle, X. Litaudon, M. Mattioli, A. L. Pecquet, Y. Peysson, G. Rey, J. L. Segui, G. Tonon, and D. Van Houtte, in *Plasma Physics and Controlled Nuclear Fusion Research 1992*, Würzburg (International Atomic Energy Agency, Vienna, 1993), Vol. 1, pp. 649–660.
[33]G. Fussmann, B. J. Green, and H. P. Zehrfeld, in *Plasma Physics and Controlled Nuclear Fusion Research 1980*, Brussels (International Atomic Energy Agency, Vienna, 1981), Vol. 1, p. 353.
[34]D. J. Sigmar, J. A. Clarke, R. V. Neidigh, and K. L. Vander Sluis, Phys. Rev. Lett. **33**, 1376 (1974).
[35]P. A. Duperrex, A. Pochelon, A. W. Edwards, and J. A. Snipes, Nucl. Fusion **32**, 1161 (1992).
[36]R. Z. Sagdeev, Rev. Mod. Phys. **51**, 1 (1979).
[37]J. D. Meiss and W. Horton, Phys. Fluids **25**, 1838 (1982).
[38]S. J. Zweben, Phys. Fluids **28**, 974 (1985).
[39]H. Johnsen, H. L. Pécseli, and J. Trulsen, Phys. Fluids **30**, 2239 (1987).
[40]A. V. Filippas, Ch. P. Ritz, A. E. Koniges, J. A. Crotinger, and P. H. Diamond, in *Proceedings of the 18th European Conference on Controlled Fusion and Plasma Physics*, Berlin, edited by P. Bachmann and D. C. Robinson (European Physical Society, Geneva, 1991), Vol. 15C, Part I, p. 309.
[41]W. Horton, R. D. Bengston, and P. J. Morrison, in *Transport, Chaos and Plasma Physics*, edited by S. Benkadda, F. Doveil, and Y. Elskens (World Scientific, London, 1994), pp. 200–212.
[42]H. D. I. Abarbanel, R. Brown, J. J. Sidorowich, and L. S. Tsimring, Rev. Mod. Phys. **65**, 1331 (1993).
[43]L. Sirovich, Physica D **37**, 126 (1985).
[44]S. Benkadda, T. Dudok de Wit, M. Endler, X. Garbet, A. Sen A. Verga, "Characterization of coherent structures in plasma edge turbulence," submitted to Phys. Rev. Lett.
[45]R. J. Vaccaro (editor), *SVD and Signal Processing* (Elsevier, Amsterdam, 1991).
[46]J.-M. Moret and Equipe Tore Supra, Nucl. Fusion **32**, 1241 (1992).
[47]Th. Dudok de Wit, Ph.D. thesis, Centre de Recherches en Physique des Plasmas, Lausanne, 1992.